Journal of Cleaner Production 140 (2017) 1399–1414

Contents lists available at ScienceDirect

Journal of Cleaner Production

journal homepage: www.elsevier.com/locate/jclepro

Desalination of shale gas produced water: A rigorous design approach for zero-liquid discharge evaporation systems

Viviani C. Onishi [a, *], Alba Carrero-Parreño [a], Juan A. Reyes-Labarta [b], Eric S. Fraga [c], José A. Caballero [b]

[a] Institute of Chemical Process Engineering, University of Alicante, Ap. Correos 99, Alicante 03080, Spain
[b] Department of Chemical Engineering, University of Alicante, Ap. Correos 99, Alicante 03080, Spain
[c] Centre for Process Systems Engineering, Department of Chemical Engineering, University College London, London WC1E 7JE, UK

ARTICLE INFO

Article history:
Received 26 August 2016
Received in revised form
24 September 2016
Accepted 5 October 2016
Available online 8 October 2016

Keywords:
Shale gas
Zero-liquid discharge (ZLD)
Single-effect evaporation (SEE)
Multiple-effect evaporation (MEE)
Mechanical vapor recompression (MVR)
Energy recovery

ABSTRACT

Shale gas has recently emerged as a promising energy source to face the increasing global demand. This paper introduces a new rigorous optimization model for the simultaneous synthesis of single and multiple-effect evaporation (SEE/MEE) systems, considering mechanical vapor recompression (MVR) and energy recovery. The proposed model has been especially developed for the desalination of high-salinity produced water from shale gas hydraulic fracturing ("*fracking*"). Its main objective is to enhance the system energy efficiency through the reduction of brine discharges. Therefore, the outflow brine salinity should be near to salt saturation conditions to achieve zero liquid discharge (ZLD). The multiple-effect superstructure is comprised by several effects of horizontal-tube falling film evaporation. Due to the inclusion of the electric-driven mechanical compressor, no other external energy source is needed in the SEE/MEE system. A more accurate process design is attained through the calculation of the overall heat transfer coefficients in function of the individual coefficients for the falling boiling film and vapor condensation. Additionally, the SEE/MEE-MVR model allows the estimation of the major geometrical characteristics of the evaporation system. The non-linear programming (NLP)-based model is optimized using the CONOPT solver under GAMS by the minimization of the process total annualized cost. Thermal analysis is carried out to evaluate the effects of the feed salinity and geometrical parameters on system heat transfer performance. The results highlight the ability of the developed model to rigorously design SEE/MEE-MVR systems by improving their cost-effectively and reaching ZLD conditions.

1. Introduction

Natural gas production from tight shale formations has recently emerged as a promising carrier to face the global energy demand. One of the main reasons relies in its supply reliability, since shale gas exploration is not conditioned by unstable foreign market-places contrarily to fossil fuel-based energy sources. Due to the rising advance in horizontal drilling and hydraulic fracturing ("*fracking*") technologies, it is projected that the shale gas production in the U.S. can reach 50% in 2035 (Xiong et al., 2016). Notwithstanding, unconventional gas production from shale rocks usually generates large amounts of high-salinity flowback and produced water, requiring efficient desalination treatment (He et al., 2014). Clearly, desalination processes for the treatment of flowback and produced water from shale gas production should be as cost-effective and environment friendly as possible (Chafidz et al., 2016).

Horizontal drilling and hydraulic fracturing demands around 10,500–21500 m^3 (3–6 million gallons) of water for a single well exploration (Ghanbari and Dehghanpour, 2016). Approximately 10–80% of the total amount of injected fluid returns to surface as flowback and produced water (Hammond and O'Grady, 2016; Huang et al., 2016). Consequently, the progress in shale gas production technologies is extremely dependent of water availability and flowback and produced water disposal and/or reuse (Nicot and Scanlon, 2012). The shale gas produced water is composed by several pollutants such as chemical additives—including surfactants, friction reducers, flow improvers, corrosion inhibitors, etc., which are used for well stimulating and releasing the gas trapped into the rock formations—and elevated concentrations of salt and

* Corresponding author.
E-mail addresses: viviani.onishi@pq.cnpq.br, viviani.onishi@ua.es (V.C. Onishi).

http://dx.doi.org/10.1016/j.jclepro.2016.10.012

other minerals (Chen and Carter, 2016). The high-salinity nature of shale gas produced water can be hazardous to the environment, justifying the development of more innovative and effective desalination processes. Nevertheless, although several works have been addressed to the optimization of water consumption (Clark et al., 2013), supply chain management (Lira-Barragán et al., 2016; Zhang et al., 2016) and carbon releases reduction (Staddon and Depledge, 2015), the desalination of high-salinity shale gas produced water has received insufficient attention.

Desalination processes widely applied in industry include membrane (reverse osmosis - RO) and thermal-based technologies, which comprises multistage flash (MSF) and single/multiple-effect evaporation (SEE/MEE) with/without thermal or mechanical vapor recompression (TVR/MVR). According to Shaffer et al. (2013), SEE/MEE systems with MVR are frequently more attractive than RO process as desalination treatment for high-salinity produced water from shale gas fracking. In fact, SEE/MEE-MVR systems frequently present lower sensitivity to the fouling problems caused by greases, requiring simpler pre-treatment processes.

Horizontal-tube falling film evaporators present numerous advantages—including more compact size and easy operation and maintenance—over other evaporation equipment such as vertical-tube falling film and forced-circulation. The horizontal-tube falling film evaporators are widely used into SEE/MEE desalination systems with/without MVR, due their higher heat transfer coefficients, lower temperature differences and film flowrates, and simpler construction (Zhao et al., 2016; Zhou et al., 2015). Other benefits include the facility of dealing with non-condensable gases, liquid distribution and fouling problems (Qiu et al., 2015; Shen et al., 2015).

The horizontal-tube falling film systems with/without MVR have been extensively studied over the past few decades. Druetta et al. (2013) have presented a NLP-based model for the optimization of MEE plants for seawater desalination. Posteriorly, the model has been extended in Druetta et al. (2014) for obtaining a specific freshwater recovery ratio, by minimizing the process total annual cost. Al-Mutaz and Wazeer (2014) have developed mathematical models to assess different MEE systems, comprising parallel/cross, backward and forward seawater feed configurations. Recently, Al-Mutaz (2015) has demonstrated that MEE systems can be more attractive than the dominant MSF (Nafey et al., 2006) and RO (Chen et al., 2015) processes, regarding energy consumption. Zhou et al. (2015) have proposed a mathematical model for MEE desalination plants at low operation temperatures. In this study, the authors have studied the influence of the thermodynamic losses—due to the boiling point elevation (BPE) and flow resistances—and some geometrical parameters on the system performance. Note that the coupling between MEE systems and MVR hasn't been considered in the above-mentioned works.

Important contributions are attributed to El-Dessouky et al (El-Dessouky et al., 2000; El-Dessouky and Ettouney, 2002). in the field of seawater desalination modelling through SEE/MEE process with MVR (and TVR). In Al-Juwayhel et al. (1997), it has been proposed a SEE system with vapor compression using heat pumps. Later, El-Dessouky et al. (2000) has introduced a comparative performance analysis between the MEE-MVR and MEE-TVR systems. The SEE model by Al-Juwayhel et al. (1997) has been expanded by Ettouney (2006) for including the determination of some equipment geometrical features during the design step. However, although mathematical models have been proposed, none of these authors have optimized the correspondent evaporation processes.

The SEE process optimization has been considered in Mussati et al. (2009), by using a mathematical programming technique. In this work, a NLP-based model for SEE systems design has been sequentially optimized by the maximization of the freshwater recovery ratio, followed by the subsequent minimization of total annual cost. Walmsley (2016) has recently proposed a new design approach based-on composite curves for evaporation systems incorporating vapor recompression. Yet, it should be remarked that the sequential nature of the methods proposed in these works cannot guarantee global optimal solutions. Moreover, all previous studies have only dealt with the problem of seawater desalination, and they have not considered ZLD conditions for the rejected brine.

ZLD application have been investigated by Thu et al. (2015), through a multiple-effect adsorption system for seawater treatment. Also, Chung et al. (2016) have applied the ZLD desalination process to the multistage membrane-based distillation process. The authors have performed a process simulation considering brine concentrate disposal near to salt (NaCl) saturation conditions. Although this process can be interesting in some aspects related to scalability, exergy and energy analyses reveal that its economic viability is strongly conditioned to the required membrane specific area. Han et al. (2016) have proposed mathematical models for the design of MVR-based evaporation systems. In their work, they have considered SEE and MEE-MVR systems for the seawater desalination, aiming to reach the ZLD condition. Nevertheless, it should be noted that the authors have only performed process simulations, which can lead to non-optimal solutions. Additionally, this work lacked an economic analysis of the processes. Although the exergy and energy analyses considered by the authors may result in extremely efficient processes, they can also generate prohibitive costs.

To address all the previously mentioned limitations, this paper introduces a new optimization model for the rigorous design of SEE/MEE systems integrating MVR and heat recovery. The model is especially developed for desalination of high-salinity produced water from shale gas hydraulic fracturing. Its main objective relies in the enhancement of process energy efficiency, by achieving high freshwater recovery ratio while reducing the brine disposals. To achieve a ZLD process, the outflow brine salinity should be near to salt saturation conditions. A multiple-effect superstructure is proposed to describe the process, containing several effects of horizontal-tube falling film evaporation. In addition, intermediate flashing tanks and a feed/distillate preheater are included in the system to improve its thermal integration. Note that the SEE/MEE-MVR system does not require an additional external power source, due to the electric-driven mechanical vapor recompression cycle. The minimization of the process total annualized cost is considered as the objective function.

The proposed mathematical model is based on the previous study presented in Onishi et al. (in press), wherein a number of SEE/MEE systems configurations (with/without multistage vapor compression) have been compared in terms of their ability to operate on ZLD conditions at different feed salinities. In the latter work, experimental correlations have been used for the estimations of overall heat transfers coefficients, which can lead to non-optimal systems design. Note that these correlations are strongly dependent of operational conditions. To surpass this shortcoming, a more precise SEE/MEE-MVR design is performed through the calculation of overall heat transfer coefficients in terms of the individual falling film coefficients for vapor condensation and vaporization. In consequence, the new NLP-based model allows the estimation of the most important geometrical characteristics of the evaporation system during the design and optimization task, which represents an important innovation. In addition, all physical properties of the process streams are considered as function of their temperature and salinity in each evaporator effect. To the best of our knowledge, this is the first work proposing ZLD application to desalination of high-salinity shale gas produced water via a rigorous SEE/MEE-MVR system design including energy recovery. Additionally, a

comprehensive thermal analysis is conducted to evaluate the effects of the feed salinity and equipment geometrical parameters on the system heat transfer performance.

This paper presents the following structure: Section 2 exhibits the detailed problem definition. Section 3 shows the proposed SEE/MEE-MVR superstructure, as well as the main features of the considered horizontal-tube falling film systems. The proposed mathematical model for the SEE/MEE-MVR systems design is developed in Section 4, while its accuracy is evaluated in a case study in Section 5. Thermal analysis of the system is also performed in this section. Lastly, the main conclusions and future directions of this study are shown in Section 6.

2. Problem statement

This study considers a SEE/MEE-MVR superstructure composed by several effects of horizontal-tube falling film evaporation, and equipment for heat exchange, mechanical compression, flash separation, mixing and pumping streams. Additionally, electricity service is also provided to drive the mechanical compressor. The goal is to develop a mathematical model for the rigorous design of SEE/MEE-MVR systems with thermal integration, aiming to achieve ZLD operation and high freshwater production. The SEE/MEE-MVR design model should also allow the estimation of the principal thermal (overall heat transfer coefficients, individual falling film coefficients for vapor condensation and vaporization, and fouling resistance) and geometrical characteristics of the evaporation system (number of tubes, tubes length and shell diameter). The model should be applied to the desalination of high-salinity produced water from shale gas extraction. Hence, its supply condition (*i.e.*, flowrate, temperature, pressure and salinity) is known, while the target state is defined by ZLD specification (*i.e.*, brine discharge salinity near to conditions of salt saturation).

The desalination of high-salinity produced water from shale gas extraction can be performed after pretreatment to remove all chemical additives, greases and sand. Usually, the technologies utilized for the shale gas produced water pretreatment include sedimentation, physical and chemical precipitation, electrocoagulation, flotation and filtration. Thus, the SEE/MEE-MVR system should provide, after appropriate water pretreatment, high freshwater recovery with minimal brine discharge. Then, produced freshwater can be safely disposed or reused in drilling and hydraulic fracturing processes of new wells. Therefore, improvement on process efficiency is also responsible by the reduction of environmental impacts related to energy use and waste disposal.

The rigorous optimization of SEE/MEE-MVR systems with heat integration is a difficult task, which is aimed at obtaining the optimal process design through the minimization of the total annualized cost. The objective function comprises the capital investment in all system equipment and operational expenses related to electric power consumption. Note that the minimum cost should correspond to the lowest electric power use and smallest heat transfer area. In general, the costs correlations are highly nonconvex and nonlinear functions of the equipment capacity. Moreover, the mathematical model presents an elevated number of degrees of freedom due to the need to simultaneously optimize all streams properties (*i.e.*, pressures, temperatures, specific enthalpies, salinities and flowrates). Also, a high number of temperature constraints are required to guarantee the adequate operation of the system, increasing further the model complexity (see Appendix A).

In the SEE/MEE-MVR optimization model, the variation of the physical properties with the temperature and salinity are considered for all process streams. Still, the overall heat transfer coefficient calculation is performed by respecting the individual coefficients for the falling boiling film and vapor condensation. Note that the current literature about desalination is based on the use of experimental data correlations for the heat transfer coefficients estimations (Al-Mutaz, 2015). As these predictions have been obtained under very specific conditions, their application in other systems can lead to imprecise results (Zhao et al., 2016). The resulting NLP-based model also allows the estimation of the major geometrical features of the evaporation system, including number of tubes, tube length, evaporator shell diameter, and fouling resistance. Evidently, these additional considerations largely increase the difficulty to solve the model in a reasonable time.

Finally, the SEE/MEE-MVR system should be operated at low temperature and pressure conditions, to avoid operational problems related to fouling and corrosion due to high salt concentration and equipment instability. The lower operational conditions present several other advantages, involving minimal thermodynamic losses, and system scaling and insulation reduction (Ettouney et al., 1999).

3. SEE/MEE-MVR superstructure

The horizontal falling film MEE-MVR superstructure with thermal integration proposed for shale gas produced water desalination is depicted in Fig. 1. The multiple-effect plant comprises several effects of horizontal-tube falling film evaporation and flashing tanks, which are placed in an intermediate way. These flashing tanks are used to enhance the process efficiency by recovering energy from the condensate vapor. Moreover, the SEE/MEE-MVR system with thermal integration contains a heat exchanger (feed/distillate preheater) used for preheating shale gas produced water (feed water), by taking advantage of the condensed vapor (distillate/freshwater) sensible energy. The SEE/MEE-MVR system operates with closed vapor recompression cycle, via a mechanical compressor powered by electricity. Therefore, the vapor stream originated in the process is superheated to supply all energy demanded for driving the SEE/MEE process. For the rigorous design, the SEE-MVR system is considered as a simplification of the MEE-MVR, including only a single horizontal-tube evaporation effect coupled to the compressor and preheater.

A backward feed configuration is considered in the SEE/MEE-MVR plant. As a result, the preheated feed water is introduced in the last effect, while the brine stream flows across the effects towards the first one. So, the last evaporation effect should be at the lowest temperature and pressure of the system. Since the pressure is monotonically reduced throughout the evaporator, pumping units—placed between each effect—are necessary for brine transport. The vapor generated in the first evaporation effect is directed to the next one, being used as the energy source. This process follows consecutively until the last effect, wherein the vapor is carried to the mechanical compressor. Observe that the produced vapor flows in the direction of the pressure and temperature drop.

The evaporation effects are composed by horizontal falling film tube-bundles for vapor condensation, nozzles for brine spraying and demisters for droplet separation. All of them are housed inside the shell, which should also contain some space for the produced saturated vapor and concentrated brine. Fig. 2 presents the main optimization variables in each evaporation effect of the horizontal falling film SEE/MEE-MVR system. Then, the feed water—henceforth corresponding to the brine stream in the effects 1 to (i-1); and, to the produced water from shale gas extraction in the last effect—is sprayed by the nozzles onto the tube-bundles, producing a thin film along their surface. On the other hand, the vapor originated from vaporization and flashing processes is introduced in the tube-side of the equipment. Accordingly, the feed water vaporization process starts by absorbing the latent heat from the

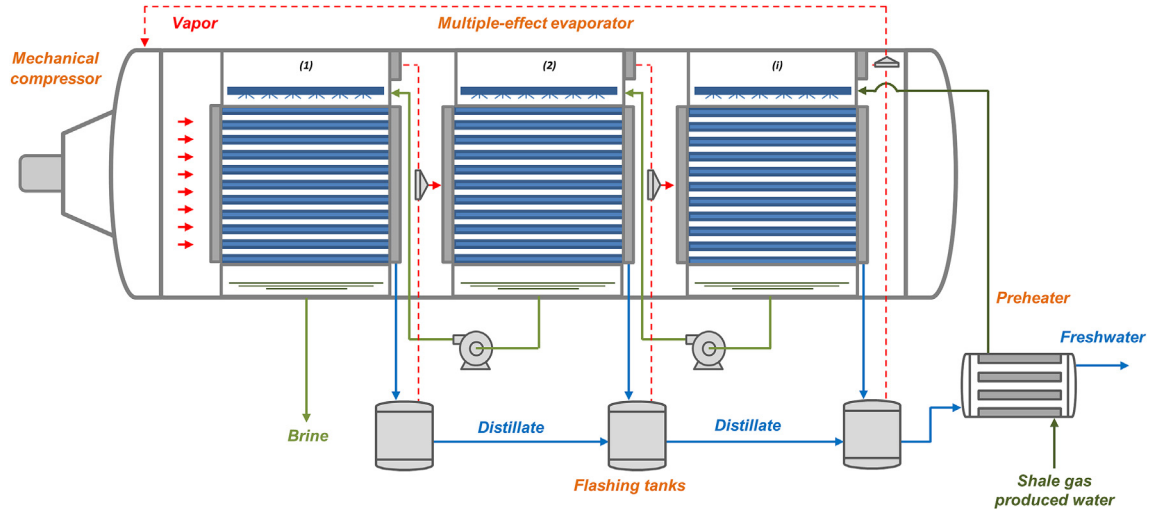

Fig. 1. MEE-MVR superstructure with horizontal falling film proposed for desalination of high-salinity produced water from shale gas production.

condensed vapor inside tubes. Thus, the condensation process into the tubes occurs due to the latent heat transfer, from the vapor to the falling film outside the tubes.

The horizontal-tube falling film configuration exhibits heat transfer coefficients higher than conventional vertical arrangements. For this reason, the horizontal-tube falling film systems present smaller heat transfers areas and, consequently, lower equipment capital cost (Qiu et al., 2015). It should be noted that the overall heat transfer coefficient is mainly governed by the falling film evaporation process. This is because the individual heat transfer coefficient for the falling boiling film is approximately half of the corresponding value for the tube-side (Li et al., 2011).

In the first evaporation effect, sensible heat promotes the temperature decreasing inside the horizontal tubes. In this case, the temperature of the condensate is changed from the inlet superheated condition until the corresponding temperature to the vapor

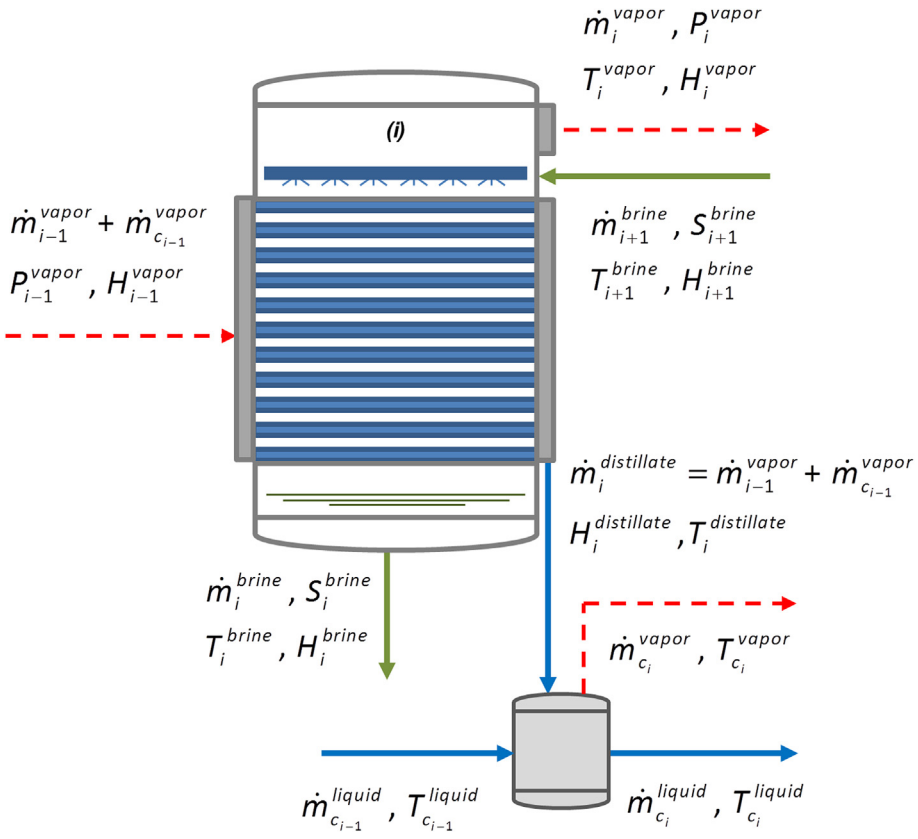

Fig. 2. Optimization variables in the *i*-effect of the horizontal falling film MEE-MVR system.

saturation pressure. Analogously to the condensation inside tubes, the evaporation process that takes place surface of the horizontal tubes is strongly affected by a number of parameters such as: (*a*) Reynolds number in the falling film (extremely influenced by the fluid velocity); (*b*) fluid physical properties (comprising the density, viscosity, specific heat and thermal conductivity); (*c*) vaporization temperature (highly influenced by the BPE); and, (*d*) geometrical characteristics (including the external tube diameter and tube pattern arrangement) (Abraham and Mani, 2015; Shen et al., 2014). Clearly, these parameters have also considerable impact on the design configuration and energy efficiency of the SEE/MEE-MVR system.

The mathematical model for the rigorous design of horizontal falling film SEE/MEE-MVR systems with thermal integration is presented in the following sections.

4. Design of SEE/MEE-MVR systems

The optimization model is based on a previous study (Onishi et al., in press), in which the performance of different SEE/MEE systems configurations (with/without multistage vapor recompression) have been compared in a large range of feed salinities. Thus, the mathematical model comprises the design equations of the evaporation system primary equipment (multiple-effect evaporator, mechanical vapor compressor, flashing tanks and preheater). The modelling formulation for these equipment is exhibited in Appendix A, including mass and energy balances for all units, temperatures constraints, and pressure and temperatures feasibilities.

Important improvements are introduced in the new model, such as the rigorous calculation of the overall heat transfer coefficient in function of the individual falling film coefficients (falling boiling film and vapor condensation) and geometrical characteristics. Moreover, a more precise estimation of the streams physical properties (viscosity, thermal conductivity, specific heat, density, vaporization latent heat, saturation pressure and temperature, and specific enthalpy) is considered by their correlations with temperature and salt concentration. The correlations to estimate thermodynamic properties and boiling point elevation (BPE) are shown in Appendix B. Additionally, the proposed model also permits the estimation of the principal geometrical features of the evaporation system (number of tubes, tubes length and shell diameter) and fouling resistance. The mathematical formulation is simplified by the following assumptions:

(i) Steady state operation.
(ii) Thermal losses can be neglected in the mechanical vapor compressor and feed/distillate preheater.
(iii) Pressure and temperature drops can be disregarded in the demister.
(iv) Pressure drop over tube-side can be neglected.
(v) Non-equilibrium allowance (NEA) can be disregarded in the evaporator system.
(vi) Vapor produced in the evaporator behave as ideal gas.
(vii) The distillate salinity is equal to zero.
(viii) The mechanical vapor recompression is an isentropic process.
(ix) Starter power to drive the mechanical vapor compressor can be neglected.
(x) Surging and choking effects can be disregarded in the mechanical vapor compressor.
(xi) Capital costs related to mixers and pumps can be neglected in the process.

The following set is needed to the development of the model: $I = \{i/i = 1,2,3,\ldots,I$ is the evaporator effect$\}$. The resulting NLP-based model is presented in the next sections.

4.1. Individual falling boiling film coefficient

The calculation of the individual falling boiling film coefficient is based the following hypotheses: (*i*) the feed water is uniformly distributed along the surface of the tubes; and, (*ii*) the falling film is formed at boiling temperature. The individual falling boiling film coefficient hff_i is given by Eq. (1).

$$hff_i = \left(Nu_i^s \cdot \kappa_i^s\right)/dex \quad \forall i \in I \tag{1}$$

In which *dex* is the external diameter of the horizontal tubes, κ_i^s is the feed thermal conductivity at boiling temperature, and Nu_i^s is the Nusselt number expressed by the following equation.

$$Nu_i^s = 0.023 \cdot \left(Re_i^s\right)^{0.8} \cdot \left(Pr_i^s\right)^{1/3} \quad \forall i \in I \tag{2}$$

The Reynolds number Re_i^s and Prandtl number Pr_i^s in the falling boiling film are calculated by Eq. (3) and Eq. (4), respectively.

$$Re_i^s = \left(v_i^s \cdot \rho_i^s \cdot dex\right)/\mu_i^s \quad \forall i \in I \tag{3}$$

$$Pr_i^s = \left(Cp_i^s \cdot \mu_i^s\right)/\kappa_i^s \quad \forall i \in I \tag{4}$$

In which v_i^s is the fluid velocity in the falling boiling film. To avoid operational problems related to fouling, corrosion and pressure drop, the falling film velocity is constrained between $1 \le v_i^s(m \cdot s^{-1}) \le 3$ (Couper et al., 2010). ρ_i^s, μ_i^s and Cp_i^s are the density, viscosity and specific heat, respectively, for the liquid phase of the feed stream estimated at boiling temperature.

4.2. Individual heat transfer coefficient for vapor condensation

The individual heat transfer coefficient for the vapor condensation hc_i is calculated analogously to the individual falling boiling film coefficient.

$$hc_i = \left(Nu_i^t \cdot \kappa_i^t\right)/din \quad \forall i \in I \tag{5}$$

In which *din* is the internal diameter of the horizontal tubes, κ_i^t is the distillate thermal conductivity, and Nu_i^t is the Nusselt number for the tube-side obtained by Eq. (6).

$$Nu_i^t = 0.023 \cdot \left(Re_i^t\right)^{0.8} \cdot \left(Pr_i^t\right)^{1/3} \quad \forall i \in I \tag{6}$$

The Reynolds number Re_i^t and Prandtl number Pr_i^t inside the horizontal tubes are expressed by the following equations.

$$Re_i^t = \left(v_i^t \cdot \rho_i^t \cdot din\right)/\mu_i^t \quad \forall i \in I \tag{7}$$

$$Pr_i^t = \left(Cp_i^t \cdot \mu_i^t\right)/\kappa_i^t \quad \forall i \in I \tag{8}$$

In which v_i^t is the fluid velocity in the falling boiling film that should be restricted to $2 \le v_i^t(m \cdot s^{-1}) \le 5$. In addition, ρ_i^t, μ_i^t and Cp_i^t indicates the density, viscosity and specific heat, respectively, of the distillate stream estimated at condensation temperature.

4.3. Overall heat transfer coefficient

The clean overall heat transfer coefficient U_i^{clean} is calculated in function of the individual falling boiling film and condensation coefficients, and geometrical features by the following equation.

$$U_i^{clean} = \left(\left(\frac{dex}{din}\right) \Big/ hc_i + rin \cdot \left(\frac{dex}{din}\right) + rout + dex \cdot \log\left(\frac{dex}{din}\right) \Big/ \left(2 \cdot \kappa^{tube}\right) + \frac{1}{hff_i}\right)^{-1} \quad \forall i \in I \tag{9}$$

$$U_i^{clean} \geq U_{i+1}^{clean} \quad \forall i \in I \tag{10}$$

In which rin• and $rout$ are the dirt resistance factor for the streams inside and outside horizontal tubes. κ^{tube} indicates the thermal conductivity of the tube. Note that Eq. (10) is necessary to guarantee the feasibility of the overall heat transfer coefficients (*i.e.*, the overall heat transfer coefficient should monotonically decrease throughout the evaporation effects).

4.4. Fouling resistance

The fouling resistance rf_i is expressed in terms of the clean and dirty overall heat transfer coefficients by Eq. (11).

$$rf_i = \left(U_i^{clean} - U_i\right) \Big/ U_i^{clean} \cdot U_i \quad \forall i \in I \tag{11}$$

To ensure the appropriate equipment design, the fouling resistance should be restricted by the following specification.

$$rf_i \geq rf_i^{design} \quad \forall i \in I \tag{12}$$

4.5. Geometrical features

The number of tubes Nt_i in each evaporator effect is estimated by Eq. (13), considering the heat transfer area A_i, external tube diameter dex and tube length L_i.

$$Nt_i = A_i/(\pi \cdot dex \cdot L_i) \quad \forall i \in I \tag{13}$$

The horizontal-tube bundle has square pattern arrangement. The tube length is expressed in terms of the external tube diameter and number of tubes (Ettouney, 2006).

$$L_i = (ftp \cdot dex \cdot Nt_i)^{0.5} \quad \forall i \in I \tag{14}$$

In which ftp is the tube pitch factor. As proposed by Ettouney (2006) this factor should be limited between 1.25 and 1.5. The evaporator shell diameter Ds_i is obtained in function of the horizontal tube length by Eq. (15).

$$Ds_i = 1.77 \cdot L_i \quad \forall i \in I \tag{15}$$

Each evaporation effect should be designed to house a tube-bundle, demister, spray nozzles, and brine. As the evaporator should be compact equipment composed by several effects, the largest diameter of these effects is considered the equipment diameter.

4.6. Heat transfer area

The total heat transfer area of the evaporator should be equal to the sum of the heat transfer areas of each effect. The total evaporator heat transfer area (A) is given by Eq. (16).

$$A = \sum_{i=1}^{I} A_i = \sum_{i=1}^{I} Q_i \cdot (U_i \cdot LMTD_i)^{-1} \tag{16}$$

In which Q_i indicates the heat requirements in each evaporator effect (Appendix A), and $LMTD_i$ is the log mean temperature difference defined by the Chen's approximation (Chen, 1987).

$$LMTD_i = \left[1/2 \cdot (\theta_{1i} \cdot \theta_{2i}) \cdot (\theta_{1i} + \theta_{2i})\right]^{\frac{1}{3}} \quad \forall i \in I \tag{17}$$

In which the temperatures differences θ_{1i} and θ_{2i} are defined by the following equations.

$$\theta_{1i} = \begin{cases} T^{sup} - T_i^{boiling} & i = 1 \\ T_i^{sat} - T_i^{boiling} & i > 1 \end{cases} \text{ and}$$

$$\theta_{2i} = \begin{cases} T_i^{distillate} - T_{i+1}^{boiling} & i = 1 \\ T_i^{sat} - T_{i+1}^{boiling} & 1 < i < I \\ T_i^{sat} - T_i^{feed} & i = I \end{cases} \tag{18}$$

The heat transfer area of the first effect is calculated in terms of the sensible and latent heat transfer areas as expressed by Eq. (19).

$$A_i = A_i^1 + A_i^2 \quad i = 1 \tag{19}$$

In which,

$$A_i^1 = \dot{m}_i^s \cdot Cp_i^{vapor} \cdot \left(T^{sup} - T_i^{distillate}\right) \Big/ \left(U^S \cdot LMTD_i\right) \quad i = 1 \tag{20}$$

$$A_i^2 = \dot{m}_i^s \cdot \left(H_i^{cv} - H_i^{distillate}\right) \Big/ U_i \cdot \left(T_i^{distillate} - T_i^{boiling}\right) \quad i = 1 \tag{21}$$

In which H_i^{cv} and H_i^{cond} are the specific enthalpies for the vapor and liquid phases of the distillate (estimated at the condensation temperature $T_i^{distillate}$), respectively. To avoid the non-uniform area distribution, the following constraints are required:

$$A_i \leq t \cdot A_{i-1} \quad i > 1 \tag{22}$$

$$A_i \geq A_{i-1} \quad i > 1 \tag{23}$$

In which the parameter t=3 is considered in this model. Though, this parameter can be chosen arbitrarily by the designer. Clearly, this restriction can be easily removed from the optimization model.

4.7. Zero-liquid discharge specification

The SEE/MEE-MVR system is designed to achieve discharge conditions near to ZLD operation. For this purpose, the brine discharge salinity should be higher than the design specification defined by the salt saturation conditions.

$$S_i^{brine} \geq S^{design} \quad i = 1 \tag{24}$$

Note that this constraint obligates that the brine discharge salinity must be at least equal to a specified minimum value. It should be highlighted that the minimum cost is always obtained for achieving the lower brine concentration.

4.8. Objective function

The minimization of the total annualized cost of the SEE/MEE-MVR system is considered as the objective function. The total annualized cost comprises the capital cost of investment in all units needed in the system, and the operational expenses related to electricity consumption.

$$\min \quad C_{total} = C_{capital} + C_{operational} \tag{25}$$

$$s.t. \quad \text{Eq. (1)–Eq. (23)}$$

$$S_1^{brine} \geq S^{design}$$

The capital investment and operational costs are given by Eq. (26) and Eq. (27), respectively.

$$C_{capital} = fac \cdot \left(\frac{CEPCI^{2015}}{CEPCI^{2003}}\right) \cdot \left((C_{PO} \cdot F_{BM} \cdot F_P)^{evaporator} + (C_{PO} \cdot F_{BM} \cdot F_P)^{compressor} + \left(\sum_{i=1}^{I} C_{POi} \cdot F_{BM} \cdot F_P\right)^{flash} + (C_{PO} \cdot F_{BM} \cdot F_P)^{preheater} \right) \tag{26}$$

$$C_{operational} = C_e \cdot W \tag{27}$$

The factor of annualization for the capital investment *fac* is calculated by the following equation (Smith, 2005):

$$fac = i \cdot (1+i)^y \cdot \left[(1+i)^y - 1\right]^{-1} \tag{28}$$

In which, i indicates the interest rate fraction (per year) and y the amortization period. The total capital cost is assessed according to the pertinent year by the CEPCI index. In Eq. (26), C_{PO} is the equipment unit cost (in kUS$) estimated by the correlations of Turton et al. (2012) (flashing tanks and preheater) and Couper et al. (2010) (mechanical compressor and evaporator). F_{BM} is a correction factor for the equipment unit cost, which correlates the construction materials with operational conditions.

5. Results and discussion

5.1. Optimal rigorous SEE/MEE-MVR design

The model is initially evaluated regarding its capability to rigorously optimize horizontal falling film SEE/MEE-MVR systems. For this purpose, two case studies related to desalination of shale gas produced water are carried out, considering the feed salinity equal to 70 g kg^{-1} (70 k ppm)—salt concentration based on real data from U.S. shale plays (Zammerilli et al., 2014)—. However, the brine discharge salinity should be equal or higher than 300 g kg^{-1} (300 k ppm) to achieve ZLD operation (Han et al., 2016). The SEE/MEE-MVR systems should have the capacity of treating 10.42 kg s^{-1} (~900 m^3 day^{-1}) of high-salinity produced water from shale gas production. The plant capacity considered in this study is based on the work of Lira-Barragán et al. (2016), which corresponds to a treatment schedule of 20 wells per year. Design parameters include: shell and tube-side velocities restricted between 1 and 3 m s^{-1} and 2–5 m s^{-1}, respectively; and, fouling resistance inside and outside the horizontal tubes equal to 1.5e-3 m^2 K kW^{-1} and 1e-3 m^2 K kW^{-1}, correspondingly. Tubes of nickel are used with thermal conductivity of 0.120 kW (m K)$^{-1}$. Operational restrictions to avoid fouling and rusting problems comprise the ideal temperature T_i^{ideal} of evaporation effects constrained at 1–100 °C, and the vapor saturation pressure P_i^{sat} limited between 1 and 200 kPa. The minimum temperature and pressure drops between evaporation effects are 0.1 °C and 0.1 kPa, respectively. Moreover, the minimum temperature approaches between the superheated vapor and distillate, as well as between brine and vapor are $\Delta T_{min}^{dist} = 2$°C and $\Delta T_{min}^{brine} = 2$°C, respectively. Additional problem data are presented in Table 1, while Fig. 1 displays the proposed superstructure for the horizontal falling film desalination plant.

5.1.1. Case study 1: SEE-MVR design

Firstly, the proposed rigorous model is used to optimize a horizontal falling film SEE-MVR system, by the minimization of the total annualized cost. The optimal configuration obtained for the SEE-MVR system exhibits a heat transfer area (and heat duty) of 659.99 m^2 (19,780.44 kW). The evaporation effect is composed by a bundle containing 3612 horizontal tubes (of 2.29 m of length), which is housed in a shell with 4.05 m of diameter. In addition, the SEE-MVR process requires a compressor with 1452.19 kW of capacity, and a preheater with 4.80 m^2 of heat transfer area (corresponding to a heat flow of 403.28 kW). Thus, the specific heat transfer area (*i.e.*, heat transfer area needed to produce 1 kg s^{-1} of water) is equal to 83.21 m^2 s kg^{-1}, resulting in a specific heat duty requirement of 2475.96 kW s kg^{-1}. Still, the system performance evaluation includes the specific work (*i.e.*, compression work needed to produce 1 kg s^{-1} of water) that is equal to 181.77 kW s kg^{-1}. Fig. 3 shows the optimal SEE-MVR process configuration, and Table 2 presents the main thermodynamic and geometrical results obtained for this case study. The total annualized cost of the process is equal to 2538 kUS$ $year^{-1}$, comprising 1303 kUS$ $year^{-1}$ related to capital cost of investment in equipment and 1235 kUS$ $year^{-1}$ to operational expenses (electric power consumption). It should be noted that the ZLD operation (brine discharge salinity at 300 g kg^{-1}) allows obtaining a distillate production of 7.99 kg s^{-1}, corresponding to 76.7% of freshwater recovery. The water production cost is equal to 10.07 US$ per cubic meter (~0.038 US$ $gallon^{-1}$) of produced freshwater, of which ~48% corresponds to electric power consumption. Furthermore, besides allowing the calculation of the main thermodynamic and geometrical characteristics of the desalination system, this new rigorous model also reduced by ~8% the total annualized cost obtained for the evaporation plant when designed using correlations to estimate overall heat transfer coefficients (Onishi et al., in press).

5.1.2. Case study 2: MEE-MVR design

Secondly, the mathematical model is used for the cost-effective optimization of the MEE-MVR design. The system is evaluated as its potential to achieve high recovery ratio of freshwater at ZLD conditions. The minimization of the total annualized cost of the desalination process is again considered as an objective function. In this case, the optimal MEE-MVR system configuration is composed by two evaporation effects with heat transfers areas (and heat duty) of 245.91 m^2 (9718.74 kW) and 216.0 m^2 (9702.28 kW). The first evaporation effect contains 1870 horizontal tubes with 1.65 m of length, while the second one needs 1715 tubes measuring 1.58 m. To house these tube-bundles, the evaporator shell diameter should be equal to 2.92 m (as commented before, the bigger effect diameter is considered to be the equipment diameter). Additionally, a mechanical vapor compressor with 823.10 kW of capacity, and a preheater with heat transfer area of 46.97 m^2 (1774.31 kW) are used in the process. Under this configuration, the system presents a specific compression work of 101.78 kW s kg^{-1}, and a specific heat transfer area (specific heat duty) of 63.70 m^2 s kg^{-1} (2430.97 kW s

Table 1
Parameters for the rigorous design of SEE/MEE-MVR systems for the desalination of shale gas produced water.

Feed water (produced water from shale gas extraction)	Mass flowrate, $\dot{m}_l^{feed}$ (kg s^{-1})	10.42
	Temperature, T_l^{feed} (°C)	25
	Salt concentration, S_l^{feed} (g kg^{-1})	70
Multiple-effect evaporator (horizontal-tube falling film)	External diameter of a single tube, *dex* (m)	0.0254
	Internal diameter of a single tube, *din* (BWG14, m)	0.0212
	Thermal conductivity of the tube, κ^{tube} (Nickel, kW (m K)$^{-1}$) [a]	0.120
Mechanical compressor (centrifugal/carbon steel)	Isentropic efficiency, η (%)	75
	Heat capacity ratio, γ	1.33
	Maximum compression ratio, CR_{max}	3
Process specifications	Brine salinity, S^{design} (g kg^{-1})	300
	Evaporator temperature range, T_i^{ideal} (°C)	1–100
	Evaporator pressure range, P_i^{sat} (kPa)	1–200
	Shell-side velocity, v_i^s (m s^{-1})	1–3
	Tube-side velocity, v_i^t (m s^{-1})	2–5
Cost data	Electricity cost [b], C_e (US$ (kW year)$^{-1}$)	850.51
	Fractional interest rate per year, *i*	0.1
	Amortization period, *y*	10

[a] Data obtained from Couper et al. (2010).
[b] Data extracted from Eurostat (European Comission, 2016) (2015 – 1st semester).

kg^{-1}). These values represent a decreasing around 44% in the specific compression work, and ~23.5% of diminution in the specific heat transfer area in comparison with Case 1 (SEE-MVR system). Fig. 4 depicts the optimal MEE-MVR system configuration, and Table 2 presents the main thermodynamic and geometrical results obtained for this case study. The total annualized cost of the MEE-MVR system is equal to 1651 kUS$ $year^{-1}$, involving 951 kUS$ $year^{-1}$ associated to capital cost and 700 kUS$ $year^{-1}$ to operational expenses. Once again, the ZLD operation allows a water production rate of 7.99 kg s^{-1}, resulting in 76.7% of freshwater recovery. The water production cost is now equal to 6.55 US$ per cubic meter (~0.025 US$ $gallon^{-1}$) of produced freshwater, of which approximately 42% are related to electric power consumption. Therefore, the multiple-effect evaporation system is around 35% more economical than the SEE-MVR system (both in terms of its total annualized cost and water production cost) for the same recovery ratio of freshwater.

It should be noted that if three evaporation effects are considered in the system, the total annualized cost is increased for 1669 kUS$ $year^{-1}$, composed by 1104 kUS$ $year^{-1}$ related to capital cost and 564 kUS$ $year^{-1}$ to operational expenses. The freshwater recovery ratio is equal to 0.77 (or 76.7%), corresponding to a water production rate of 7.99 kg s^{-1}. Thus, the freshwater production cost is increased for 6.62 US$ m^{-3} (~0.025 US$ $gallon^{-1}$), of which ~34% are associated to electric power consumption. Hence, in spite of the diminution in the operational expenses, the increase in capital costs—due to the increment in specific heat transfer area for 87.24 m^2 s kg^{-1}—makes the three-effect evaporator less advantageous than the previous two-effect system. Nevertheless, the three-effect MEE-MVR system is ~34% less expensive than the SEE-MVR system. Note that the SEE-MVR system is usually the preferred industrial process for shale gas produced water desalination.

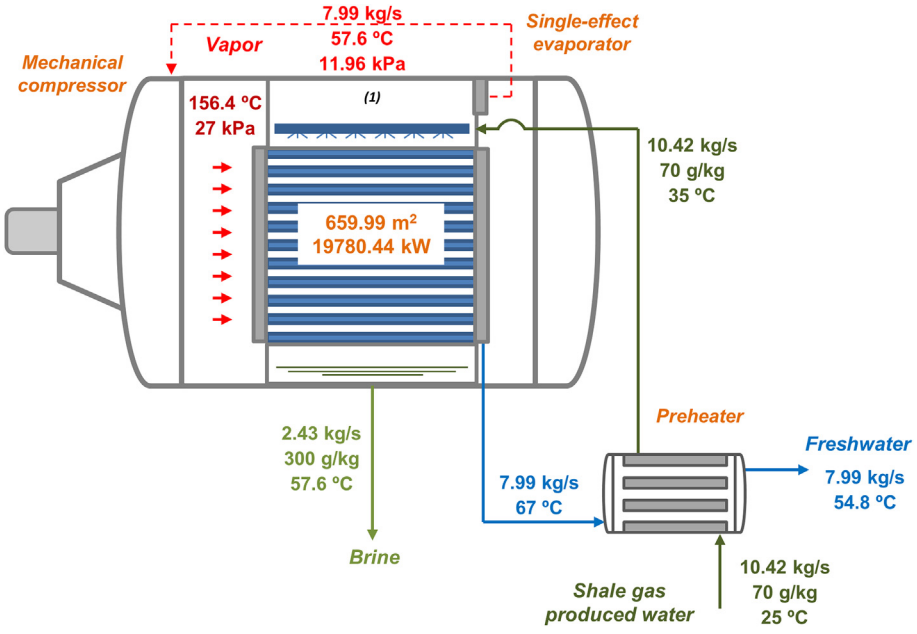

Fig. 3. Optimal process configuration obtained for the horizontal falling film SEE-MVR system.

Table 2
Optimal thermodynamic and geometrical results obtained for the case studies.

System features	SEE-MVR system	MEE-MVR system	
		1st effect	2nd effect
hff_i, kW (m^2 K)$^{-1}$	5.89	8.63	7.91
Pr_i^s	4.98	2.89	2.29
Re_i^s	5.25e+4	1e+5	1e+5
Nu_i^s	234.19	327.33	303.17
v_i^s, m s^{-1}	2	2.34	1.57
hc_i, kW (m^2 K)$^{-1}$	9.67	13.50	13.00
Pr_i^t	1.37	1.55	1.30
Re_i^t	1.31e+5	1.79e+5	1.87e+5
Nu_i^t	316.55	424.86	414.20
v_i^t, m s^{-1}	3	5	4.3
rf_i, m^2 K kW^{-1}	3e-3	2e-3	2e-3
U_i^{clean}, kW m^{-2}K^{-1}	3.17	4.43	4.17
U_i, kW m^{-2}K^{-1}	3.14	4.38	4.13
Nt_i	3612	1870	1715
L_i, m	2.29	1.65	1.58
Ds_i, m	4.05	2.92	2.79
$LMTD_i$	81.87	51.14	10.87
BPE_i, °C	6.66	8.19	2.04
$C_{capital}$, kUS$ year^{-1}	1303	951	
$C_{operational}$, kUS$ year^{-1}	1235	700	
C_{total}, kUS$ year^{-1}	2538	1651	
$C_{freshwater}$, US$ gallon^{-1}[a]	~0.038	~0.025	

[a] It is considered the U.S. gallon.

The developed NLP-based model for the rigorous optimization of SEE/MEE-MVR system design have been implemented in GAMS (version 24.7.1), and solved by CONOPT (Drud, 1996). All case studies have been solved with a personal computer with an Intel Core i5-2520M 2.5 GHz processor and 8 GB RAM running Windows 8.1. The CPU time did not exceed 2 s for all cases. In Case study 1, the mathematical model for the SEE-MVR design contains 73 continuous variables, 76 constraints with 209 Jacobian elements (non-zeros), in which 91 are nonlinear. In Case 2, the optimization model for the MEE-MVR design contains 131 continuous variables, 143 constraints with 403 Jacobian elements (non-zeros), in which 177 are nonlinear.

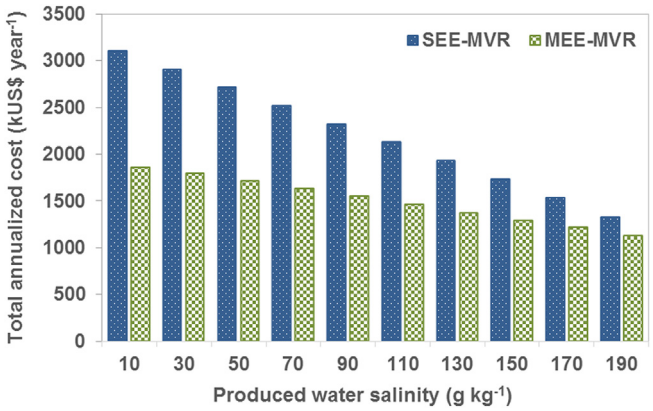

Fig. 5. Comparative effect of produced water salinity on the total annualized cost of SEE/MEE-MVR systems.

5.2. Parametric study of the effect of produced water salinity on the system performance

The effect of shale gas produced water salinity on the SEE/MEE-MVR systems performance is assessed in a range of 10–190 g kg^{-1} of feed salt concentration. In all cases, the SEE/MEE-MVR systems are designed to achieve ZLD operation by considering the brine discharge salinity at least equal to 300 g kg^{-1}. Moreover, the desalination plants should have the treatment capacity of 10.42 kg s^{-1} of produced water. Fig. 5 shows the comparative effect of the feed salinity on the total annualized cost of the SEE-MVR and MEE-MVR processes. It should be highlighted that both systems present lower process total annualized cost under higher feed salinities. As consequence of the compressor capacity and heat transfer areas lessening, operational expenses related to electricity consumption, and the capital cost of investment in equipment will also decrease with the feed salinity augmentation. Nonetheless, the costs of freshwater production and electric power consumption

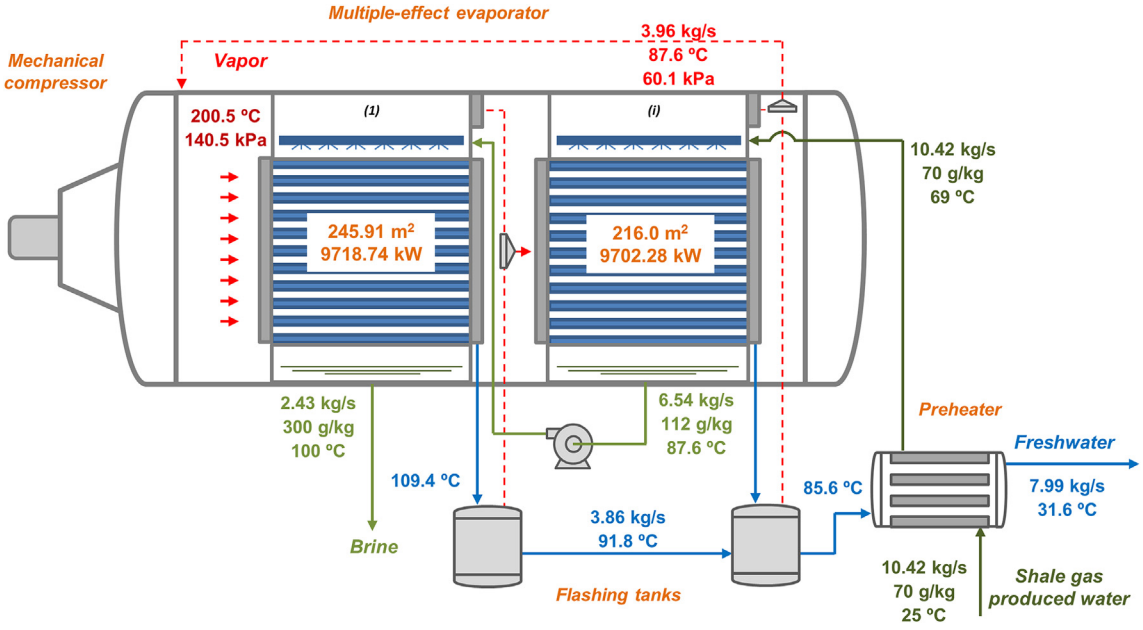

Fig. 4. Optimal process configuration obtained for the horizontal falling film MEE-MVR system.

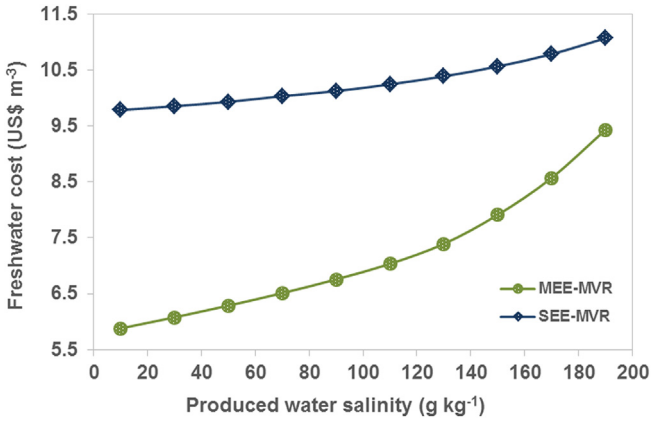

Fig. 6. Comparative effect of produced water salinity on the freshwater production cost of the SEE/MEE-MVR systems.

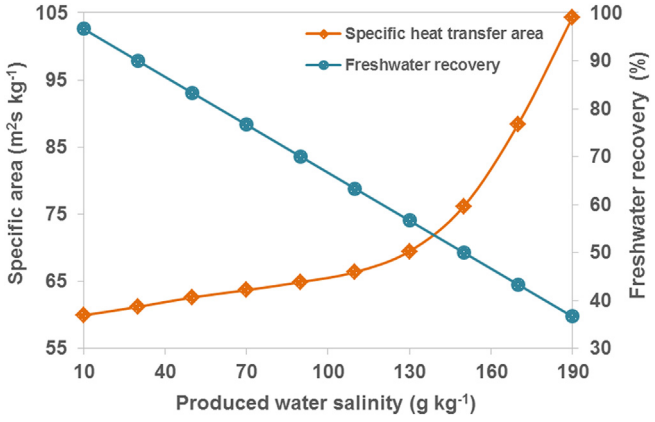

Fig. 7. Comparative effect of produced water salinity on the specific heat transfer area and freshwater recovery for the MEE-MVR system.

increase as higher feed salinities are considered in process. In this way, freshwater production cost for the MEE-MVR system is about 40% lower than the result obtained for the SEE-MVR system at salinity of 10 g kg^{-1}, and ~15% more economical at 190 g kg^{-1} of feed salt concentration. Fig. 6 displays the comparative effect of the feed salinity on freshwater production cost of the SEE-MVR and MEE-MVR processes. Observe that this behavior is mainly due to the higher freshwater recovery ratio, allied to the smaller specific heat transfer areas and specific compression work obtained at lower produced water salinities. Fig. 7 shows the effect of the feed salinity on the specific heat transfer area and freshwater recovery for the MEE-MVR system. The effect of the feed salinity on the SEE-MVR system performance is analogous to the MEE-MVR process (for this reason, it will not be shown here). However, in all cases the MEE-MVR system presents reduced water production costs in comparison with the SEE-MVR process, as shown in Fig. 6. Therefore, the obtained results have revealed that the MEE-MVR system is always more thermo-economically advantageous than the SEE-MVR system under distinct salinity scenarios.

5.3. Parametric study of the effect of geometrical characteristics on the system performance

The overall heat transfer coefficient is one of the most important parameters in the SEE/MEE-MVR system design. This coefficient is strongly dependent of the geometrical features of the evaporation equipment. So, in order to evaluate this dependence and the correspondent effect of the geometrical characteristics on the SEE/MEE-MVR system performance, two different standard tube external diameters (0.02540 m and 0.01905 m) are considered for optimization. Thus, both SEE-MVR and MEE-MVR systems are designed considering distinct tube internal diameters (*i.e.*, distinct standard BWG—Birmingham Wire Gauge—tubes) for each tube external diameter. In all cases, the treatment capacity of the desalination plant should be equal to 10.42 kg s^{-1} of shale gas produced water. Moreover, the feed salinity is considered to be equal to 70 g kg^{-1}, and the brine discharge salinity should be at least equal to 300 g kg^{-1} (to achieve ZLD conditions). Table 3 presents the results obtained for the performance parameters of the MEE-MVR system for different horizontal-tube diameters. Again, the effect of the geometrical features on the SEE-MVR system performance is analogous to the MEE-MVR process and for this reason; the detailed results will not be shown here.

Note that the overall heat transfer coefficient is increased as the tube external diameter is reduced (0.01905 m), and the internal diameter is augmented (higher values for overall clean and dirty heat transfer coefficients found for BWG 18, or *din* equal to 0.0166 m). Also, the individual heat transfer coefficients for vapor condensation (for both effects) are lower as the tube internal diameter is enlarged in the system. Consequently, the heat transfer areas for each effect, as well as the specific total heat transfer area decrease as the tube internal diameter is increased (because the overall clean and dirty heat transfer coefficients are proportionally augmented with the diminution of the tube internal diameter). Fig. 8 displays the effect of the overall heat transfer coefficient on the specific heat transfer area for the SEE-MVR system, while Fig. 9 depicts the same effect for the MEE-MVR system under consideration of different tube external diameters.

As consequence of the heat transfer area lessening, the geometrical parameters related to tubes length, evaporator shell diameter and number of tubes are also reduced in the system. Obviously, the total annualized cost and freshwater production cost will decrease as the heat transfer area rises (~7% of reduction in the total annualized cost for *dex* = 0.02540 m, and ~6% for *dex* = 0.01905 m). Fig. 10 shows the variation in the process total annualized cost, and freshwater production cost as function of the tube internal diameter changes in the SEE/MEE-MVR systems. However, the operational expenses related to electricity consumption is not affected by the variation in the geometrical parameters of the evaporator (1235 kUS$ $year^{-1}$ for the SEE-MVR system, and 700 kUS$ $year^{-1}$ for the MEE-MVR system). This is because only capital costs are affected by the variation of the geometrical characteristics of the SEE/MEE-MVR systems. Therefore, the optimal solution found for the horizontal falling film SEE-MVR system is equal to 2470 kUS$ $year^{-1}$ (1235 kUS$ $year^{-1}$ for both operational expenses and capital costs), under consideration of the external diameter equal to 0.01905 m and BWG 18 (*din* = 0.0166 m). For the MEE-MVR system, the optimal solution is equal to 1552 kUS$ $year^{-1}$ (700 kUS$ $year^{-1}$ related to operational expenses, and 852 kUS$ $year^{-1}$ associated to capital costs), obtained for *dex* = 0.01905 m and *din* = 0.0166 m. Hence, the horizontal falling film MEE-MVR system is approximately 37% more economical than the SEE-MEE system.

6. Conclusions

A new mathematical model for the rigorous design of horizontal falling film SEE/MEE systems is proposed, integrating MVR and heat recovery. The model is particularly developed for the desalination of the high-salinity shale gas produced water. Thus, the system design is aimed at the enhancement of energy efficiency by

Table 3
Effect of geometrical characteristics on the performance of the MEE-MVR system.

BWG	*din* (m)	U_1^{clean} (kW m^{-2}K^{-1})	U_2^{clean} (kW m^{-2}K^{-1})	hc_1 (kW (m^2 K)$^{-1}$)	hc_2 (kW (m^2 K)$^{-1}$)	A_1 (m^2)	A_2 (m^2)	Nt_1	Nt_2	$C_{capital}$ (kUS$ year^{-1})
dex(m)	0.02540									
8	0.0170	3.75	3.56	14.11	13.61	285.44	253.10	2066	1907	1044
9	0.0179	3.89	3.69	13.97	13.47	275.93	244.17	2020	1861	1022
10	0.0186	4.00	3.79	13.86	13.36	268.97	237.64	1985	1828	1005
11	0.0193	4.12	3.89	13.76	13.26	262.35	231.43	1953	1796	990
12	0.0199	4.21	3.98	13.67	13.17	256.93	226.34	1926	1770	978
13	0.0206	4.33	4.08	13.58	13.08	250.88	220.67	1895	1740	964
14	0.0212	4.43	4.17	13.50	13.00	245.91	216.00	1870	1715	952
15	0.0217	4.51	4.24	13.44	12.94	241.90	212.24	1850	1695	943
16	0.0221	4.58	4.30	13.39	12.89	238.79	209.32	1834	1680	936
17	0.0225	4.64	4.36	13.34	12.84	235.75	206.47	1818	1665	929
18	0.0229	4.71	4.42	13.30	12.80	232.78	203.68	1803	1650	922
BWG	*din* (m)	U_1^{clean} (kW m^{-2}K^{-1})	U_2^{clean} (kW m^{-2}K^{-1})	hc_1 (kW (m^2 K)$^{-1}$)	hc_2 (kW (m^2 K)$^{-1}$)	A_1 (m^2)	A_2 (m^2)	Nt_1	Nt_2	$C_{capital}$ (kUS$ year^{-1})
dex(m)	0.01905									
10	1.22	4.33	4.17	15.08	14.58	251.28	216.29	2784	2520	959
11	1.29	4.50	4.34	14.91	14.41	242.50	208.05	2719	2455	939
12	1.35	4.65	4.48	14.78	14.28	235.50	201.48	2667	2403	922
13	1.42	4.83	4.64	14.63	14.13	227.87	194.31	2609	2346	905
14	1.48	4.98	4.79	14.51	14.01	221.73	188.54	2562	2299	890
15	1.54	5.14	4.93	14.39	13.89	215.93	183.09	2517	2255	877
16	1.57	5.21	5.00	14.34	13.84	213.15	180.48	2495	2233	871
17	1.61	5.32	5.10	14.27	13.77	209.55	177.10	2467	2205	862
18	1.66	5.45	5.22	14.18	13.68	205.21	173.03	2433	2171	852

reducing brine disposals. To achieve ZLD operation, the brine discharge salinity should be close to salt saturation conditions. A multiple-effect superstructure is developed for the process optimization, comprising several horizontal-tube falling film effects. Additionally, intermediate flashing tanks and a feed/distillate preheater are considered in the SEE/MEE-MVR system to further improve its energy recovery. A backward feed configuration is considered in the SEE/MEE-MVR desalination plant. As a result, the preheated feed water is introduced in the last effect, while the brine stream flows across the effects towards the first one. The process requires no other energy source than the electricity required to drive the mechanical vapor compressor. The minimization of the process total annualized cost is considered as the objective function, accounting for operational expenses related to electric power consumption and capital cost of investment in equipment.

The rigorous optimization is performed by the calculation of the overall heat transfer coefficient in terms of geometrical characteristics and the individual falling film coefficients for vaporization (falling boiling film) and condensation. Thus, the fluids dynamic is considered by the calculation of the dimensionless numbers of Reynolds, Prandtl and Nusselt. Still, all streams physical properties are estimated by correlating the temperatures and salinities in each evaporation effect. Furthermore, the more precise NLP-based model allows the estimation of the major geometrical characteristics of the evaporation system, including number of tubes, evaporator shell diameter and tubes length.

The rigorous optimization of horizontal falling film SEE/MEE-MVR systems with heat integration is a difficult task. The main reasons include the highly nonlinear and non-convex character of the costs correlations, and the elevated number of degrees of freedom of the model (due to the need to simultaneously optimize all streams properties). In addition, an elevated number of temperature constraints are required to ensure the adequate operation

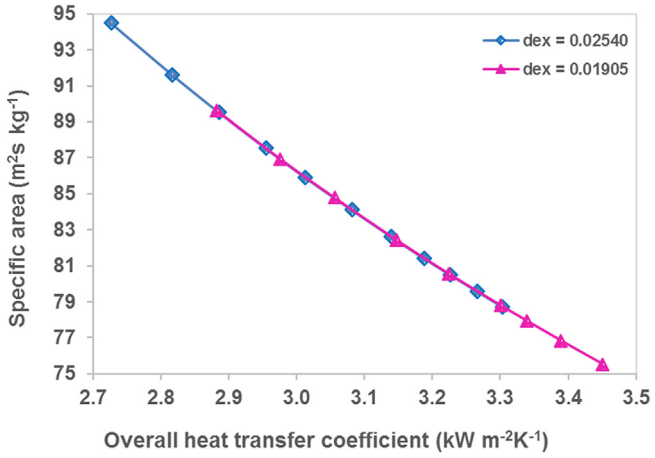

Fig. 8. Effect of the overall heat transfer coefficient on the specific heat transfer area of the SEE-MVR system for different tube external diameters.

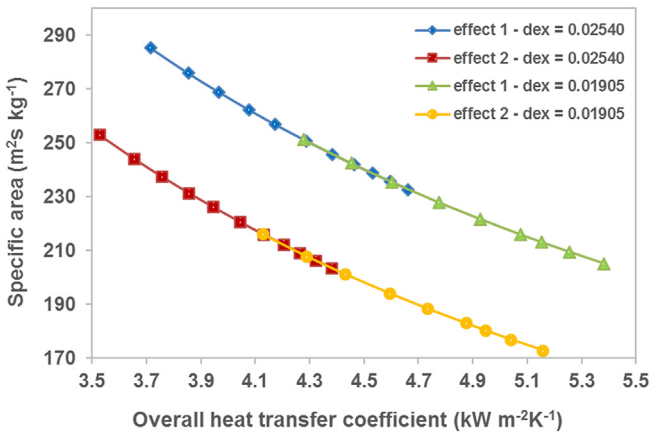

Fig. 9. Effect of the overall heat transfer coefficient on the specific heat transfer area of the MEE-MVR system for different tube external diameters and evaporator steps.

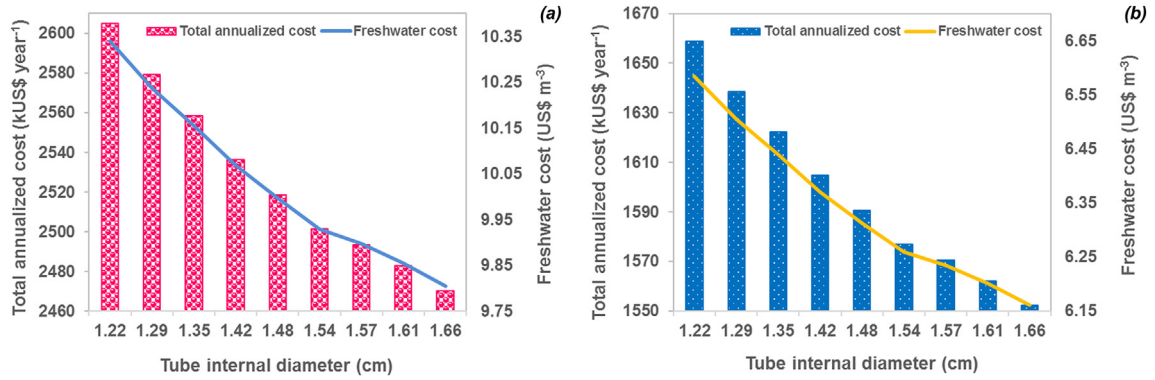

Fig. 10. Effect of the tube internal diameter variation on the total annualized cost of the process, and freshwater production cost for: (*a*) horizontal falling film SEE-MVR system; and, (*b*) horizontal falling film MEE-MVR system.

of the SEE/MEE-MVR system, increasing the model complexity. It should be remarked that the evaporation system should be operated at low pressure and temperature conditions, to avoid operational problems associated to fouling and corrosion due to high salt concentration and equipment instability.

Initially, the model is evaluated regarding its ability to rigorously optimize horizontal falling film SEE/MEE-MVR systems. The MEE-MVR system has been found to be the most beneficial process for shale gas produced water desalination with salinity of 70 g kg^{-1}. Thus, the MEE-MVR system is ~35% less expensive than the SEE-MVR system (both in terms of its total annualized cost and water production cost) for the same freshwater recovery (76.7%), and water production rate of 7.99 kg s^{-1}. The freshwater production cost is equal to ~0.025 US$ per gallon (6.55 US$ m^{-3}) of the produced water. Moreover, results found for the SEE-MVR design show that besides allowing the calculation of the main thermodynamic and geometrical characteristics of the system, the total annualized cost obtained from the new rigorous model is ~8% lower than the value estimated by a previous model based on correlations.

Afterwards, the effect of produced water salinity on the SEE/MEE-MVR system performance is assessed in a large range of salt concentrations in the feed (10–190 g kg^{-1}). Again, the MEE-MVR system has been the most advantageous desalination process under distinct salinity scenarios. Thus, freshwater production cost for the MEE-MVR system is ~40% lower than the correspondent SEE-MVR system at 10 g kg^{-1} (5.88 US$ m^{-3} *vs* 9.79 US$ m^{-3}), and ~15% inferior at 190 g kg^{-1} of feed salt concentration (9.43 US$ m^{-3} *vs* 11.07 US$ m^{-3}).

Lastly, a comprehensive thermal analysis has been carried out to evaluate the effects of the equipment geometrical parameters on the system heat transfer performance. The results obtained have once again emphasized that the horizontal falling film MEE-MVR system should be chosen as desalination treatment for shale gas produced water. In this case, the savings in process costs is around 37% when compared with the SEE-MVR at the same conditions. It should be highlighted that in all cases studied, the ZLD condition has been achieved (*i.e.*, brine discharge salinity at 300 g kg^{-1}), which has allowed obtaining the high freshwater recovery ratio of 0.77.

Despite the significant results obtained in this work, further technology development is still required to guarantee the best alternatives for desalination of high-salinity shale gas produced water. In order to achieve a more environment friendly process, future works should consider the inclusion of renewable energy sources to drive the mechanical vapor compression process, as well as life cycle assessment (LCA) to identify the optimal trade-off between economic and environmental objectives.

Acknowledgements

This project has received funding from the European Union's Horizon 2020 Research and Innovation Programme under grant agreement No. 640979. The authors also acknowledge financial support from the National Council for Scientific and Technological Development of Brazil (CNPq), under process No. 233953/2014-0.

Nomenclature

Roman letters

A	Heat transfer area, m^2
C	Cost, kUS$ $year^{-1}$
C_e	Cost parameter for electricity, US$ (kW year)$^{-1}$
Cp	Specific heat, kJ (kg °C)$^{-1}$
CPO	Cost of equipment unit, kUS$
CR_{max}	Maximum compression ratio
dex	External diameter of a single tube, m
din	Internal diameter of a single tube, m
Ds	Evaporator shell diameter, m
fac	Factor of annualized capital cost
FBM	Correction factor for the capital cost
FP	Parameter for the capital cost estimation
ftp	Tube pitch factor
H	Specific enthalpy, kJ kg^{-1}
hc	Individual heat transfer coefficient for the vapor condensation, kW (m^2 K)$^{-1}$
hff	Individual falling boiling film coefficient, kW (m^2 K)$^{-1}$
i	Fractional interest rate per year
L	Tube length, m
LMTD	Logarithmic mean temperature difference
$\dot{m}$	Mass flowrate, kg s^{-1}
Nt	Number of tubes
Nu	Nusselt number
P	Pressure, kPa
Pr	Prandtl number
ΔP_{min}	Minimum pressure approach, kPa
Q	Heat flow, kW
Re	Reynolds number
rf	Fouling resistance, m^2 K kW^{-1}

$rin•$	Dirt resistance factor inside tubes, m^2 K kW^{-1}
$rout$	Dirt resistance factor outside tubes, m^2 K kW^{-1}
S	Salinity, g kg^{-1}
T	Temperature, °C
t	Retention time in the flash tanks, min
ΔT_{min}	Minimum temperature approach, °C
U	Overall heat transfer coefficient, kW $m^{-2}K^{-1}$
V	Volume, m^3
v	Velocity, m s^{-1}
X^{salt}	Salt mass fraction
y	Number of years
W	Compression work, kW

Subscripts

i	Evaporator effects

Superscript

cv	Distillate vapor
is	Isentropic
mix	Mixture
s	Evaporator shell-side
sat	Saturated vapor
sup	Superheated vapor
t	Evaporator tube-side

Acronyms

BPE	Boiling Point Elevation
BWG	Birmingham Wire Gauge
CEPCI	Chemical Engineering Plant Cost Index
GAMS	General Algebraic Modelling System
MEE	Multiple-Effect Evaporation
MSF	Multistage Flash
MVR	Mechanical Vapor Recompression
NEA	Non-Equilibrium Allowance
NLP	Nonlinear Programming
RO	Reverse Osmosis
SEE	Single-Effect Evaporation
TVR	Thermal Vapor Recompression
ZLD	Zero Liquid Discharge

Greek letters

γ	Heat capacity ratio
η	Isentropic efficiency
θ	Temperatures difference, °C
κ	Thermal conductivity, kW (m K)$^{-1}$
κ^{tube}	Thermal conductivity of the tube, kW (m K)$^{-1}$
λ	Latent heat of vaporization, kJ kg^{-1}
μ	Viscosity, kg (m s)$^{-1}$
ρ	Density, kg m^{-3}

Appendix A. Mathematical formulation for equipment design

A.1 Mechanical vapor compressor design

The mechanical vapor compressor is designed using the following mathematical formulation.

Isentropic temperature. The isentropic temperature of the superheated vapor is expressed by the equation:

$$T^{is} = \left(T_i^{mix} + 273.15\right) \cdot \left(P^{sup} \Big/ P_i^{vapor}\right)^{\frac{\gamma-1}{\gamma}} - 273.15 \quad i = I \tag{A.1}$$

In which γ indicates the heat capacity ratio and P_I^{vapor} is the vapor pressure in the last effect. The superheated vapor pressure P^{sup} should be restricted to a maximum compression ratio CR_{max}:

$$P^{sup} \leq CR_{\max} \cdot P_i^{vapor} \quad i = I \tag{A.2}$$

Superheated vapor temperature. The superheated vapor temperature from the compressor is given by Eq. (A.3).

$$T^{sup} = T_i^{mix} + \frac{1}{\eta} \cdot \left(T^{is} - T_i^{mix}\right) \quad i = I \tag{A.3}$$

In which η represents the compressor isentropic efficiency.

Constraints on pressures and temperatures. The pressures and temperatures in the outlet of the compressor should be higher than in the inlet of this equipment.

$$T^{sup} \geq T_i^{mix} \quad i = I \tag{A.4}$$

$$P^{sup} \geq P_i^{vapor} \quad i = I \tag{A.5}$$

Compression work. The compression work is calculated in function of the difference between the enthalpies of the superheated vapor and the inlet vapor compressor.

$$W = \dot{m}^{sup} \cdot \left(H^{sup} - H_i^{vapor}\right) \quad i = I \tag{A.6}$$

In which H^{sup} and H_i^{vapor} are the vapor specific enthalpies estimated at outlet (T^{sup}) and inlet (T_I^{mix}) temperatures of the compressor, respectively. The correlations for the estimation of the vapor and liquid specific enthalpies are presented in Appendix B.

A.2 Flashing tanks design

The flashing tanks are designed using the following formulation.

Mass balances. The mass balances in an i-flashing tank are expressed by Eq. (A.7) and Eq. (A.8).

$$\dot{m}^{sup} = \dot{m}_{c_i}^{vapor} + \dot{m}_{c_i}^{liquid} \quad i = 1 \tag{A.7}$$

$$\dot{m}_{i-1}^{vapor} + \dot{m}_{c_{i-1}}^{vapor} + \dot{m}_{c_{i-1}}^{liquid} = \dot{m}_{c_i}^{vapor} + \dot{m}_{c_i}^{liquid} \quad i > 1 \tag{A.8}$$

In which $\dot{m}_{c_i}^{vapor}$ and $\dot{m}_{c_i}^{liquid}$ are the mass flowrates of the flashed off vapor phase and liquid phase of the distillate, respectively.

Energy balances. The energy balances in the flashing tanks are given by the following equations:

$$\dot{m}^{sup} \cdot H_i^{distillate} = \dot{m}_{c_i}^{vapor} \cdot H_{c_i}^{vapor} + \dot{m}_{c_i}^{liquid} \cdot H_{c_i}^{liquid} \quad i = 1 \tag{A.9}$$

$$\left(\dot{m}_{i-1}^{vapor} + \dot{m}_{c_{i-1}}^{vapor}\right) \cdot H_i^{distillate} + \dot{m}_{c_{i-1}}^{liquid} \cdot H_{c_{i-1}}^{liquid} = \dot{m}_{c_i}^{vapor} \cdot H_{c_i}^{vapor} + \dot{m}_{c_i}^{liquid} \cdot H_{c_i}^{liquid} \quad i > 1 \tag{A.10}$$

In which $H_i^{distillate}$ and $H_{c_i}^{liquid}$ are the liquid specific enthalpies estimated at condensation temperature $T_i^{distillate}$ and ideal temperature T_i^{ideal}, respectively. The vapor specific enthalpy $H_{c_i}^{vapor}$ is calculated at ideal temperature (Appendix B).

Flashing tank capacity. The volume of each flashing tank is estimated by the equations:

$$V_i^{flash} = \left(\dot{m}_i^{spv} \cdot t\right) \Big/ \rho_i \quad i = 1 \tag{A.11}$$

$$V_i^{flash} = \left(\dot{m}_{i-1}^{vapor} + \dot{m}_{c_{i-1}}^{liquid}\right) \cdot t \Big/ \rho_i \quad i > 1 \tag{A.12}$$

In which t is the time of retention and ρ_i is the distillate density. The correlations for the estimation of all streams physical properties are presented in Appendix B.

A.3 Preheater design

The feed/distillate preheater is modeled with the following mathematical formulation.

Energy balance. The energy balance in the feed/distillate preheater is given by Eq. (A.13).

$$\dot{m}_{c_i}^{liquid}\cdot Cp_i^{distillate}\cdot\left(T_i^{ideal}-T_{out}^{freshwater}\right) = \dot{m}_{in}^{feed}\cdot Cp_{in}^{feed}\cdot\left(T_i^{feed}-T_{in}^{feed}\right)\quad i=I \tag{A.13}$$

In which T_{in}^{feed} indicates the feed temperature (shale gas produced water), and $T_{out}^{freshwater}$ is the freshwater temperature. $Cp_i^{distillate}$ and Cp_{in}^{feed} are the liquid specific heats of the distillate and feed water (Appendix B), respectively.

Heat transfer area. The heat transfer area A of the preheater is obtained by Eq. (A.14).

$$A=\dot{m}_{c_i}^{liquid}\cdot Cp_i^{distillate}\cdot\left(T_i^{ideal}-T_{out}^{freshwater}\right)\Big/(U\cdot LMTD)\quad i=I \tag{A.14}$$

In which the overall heat transfer coefficient U is estimated by the correlation (Al-Mutaz and Wazeer, 2014):

$$U=0.001\cdot\left(1939.4+1.40562\cdot T_l^{ideal}-0.00207525\cdot\left(T_l^{ideal}\right)^2+0.0023186\cdot\left(T_l^{ideal}\right)^3\right) \tag{A.15}$$

The log mean temperature difference $LMTD$ in the preheater is obtained by the Chen's approximation (Chen, 1987):

$$LMTD_i=\left[1/2\cdot(\theta_{1i}\cdot\theta_{2i})\cdot(\theta_{1i}+\theta_{2i})\right]^{\frac{1}{3}}\quad\forall i\in I \tag{A.16}$$

In which,

$$\theta=T_i^{ideal}-T_i^{feed}\quad i=I\ \text{ and }\ \theta_2=T_{out}^{freshwater}-T_{in}^{feed} \tag{A.17}$$

A.4 Multiple-effect evaporator design

The horizontal falling film MEE is modeled according the following equations.

Mass balances. The mass balances in each effect of the evaporator are given by:

$$\begin{cases}\dot{m}_{i+1}^{brine}=\dot{m}_i^{brine}+\dot{m}_i^{vapor}\\ \dot{m}_{i+1}^{brine}\cdot S_{i+1}^{brine}=\dot{m}_i^{brine}\cdot S_i^{brine}\end{cases}\quad 1\le i\le I-1 \tag{A.18}$$

$$\begin{cases}\dot{m}_i^{feed}=\dot{m}_i^{brine}+\dot{m}_i^{vapor}\\ \dot{m}_i^{feed}\cdot S_{in}^{feed\_water}=\dot{m}_i^{brine}\cdot S_i^{brine}\end{cases}\quad i=I \tag{A.19}$$

Brine temperature. The temperature of the brine in each evaporation effect i is given by Eq. (A.20).

$$T_i^{brine}=T_i^{ideal}+BPE_i\quad\forall\, i\in I \tag{A.20}$$

In which BPE_i indicates the boiling point elevation (Appendix B).

Energy balances. The overall energy balances in each evaporation effect is given by the following equations.

$$Q_i+\dot{m}_{i+1}^{brine}\cdot H_{i+1}^{brine}=\dot{m}_i^{brine}\cdot H_i^{brine}+\dot{m}_i^{vapor}\cdot H_i^{vapor}\quad i<I \tag{A.21}$$

$$Q_i+\dot{m}^{feed}\cdot H_i^{feed}=\dot{m}_i^{brine}\cdot H_i^{brine}+\dot{m}_i^{vapor}\cdot H_i^{vapor}\quad i=I \tag{A.22}$$

Heat requirements. The heat requirements Q_i in each evaporation effect is given by the following equations.

$$Q_i=\dot{m}^{sup}\cdot Cp^{vapor}\cdot\left(T^{sup}-T_i^{distillate}\right)+\dot{m}^{sup}\cdot\left(H_i^{cv}-H_i^{distillate}\right)\quad i=1 \tag{A.23}$$

$$Q_i=\left(\dot{m}_{i-1}^{vapor}+\dot{m}_{c_{i-1}}^{vapor}\right)\cdot\lambda_i\quad i>1 \tag{A.24}$$

In which λ_i is the latent heat of vaporization (Appendix B). Note that $\dot{m}^{sup}$ represents the total mass flowrate of the vapor throughout the compressor:

$$\dot{m}^{sup}=\dot{m}_i^{vapor}+\dot{m}_{c_i}^{vapor}\quad i=I \tag{A.25}$$

In which $\dot{m}_i^{vapor}$ and $\dot{m}_{c_i}^{vapor}$ are the vapor and flashed off condensate vapor from the last evaporation effect, respectively.

Pressure feasibility. The vapor pressure should decrease monotonically throughout the different evaporation effects. In addition, the vapor pressure in each effect should be equal to the saturated vapor of the following effect. These pressure restrictions are guaranteed by the formulation:

$$P_i^{vapor}\ge P_{i+1}^{vapor}+\Delta P_{\min}\quad i<I \tag{A.26}$$

$$P_i^{vapor}=P_{i+1}^{sat}\quad i<I \tag{A.27}$$

Temperature constraints. Constraints on temperature are needed to avoid temperature crossovers in the effects of evaporation. These temperature constraints are given by the following equations.

$$\begin{aligned}&T^{sup}\ge T_i^{distillate}+\Delta T_{\min}^1\quad i=1\\ &T_{i-1}^{brine}\ge T_i^{distillate}+\Delta T_{\min}^1\quad i>1\end{aligned} \tag{A.28}$$

$$\begin{aligned}&T_i^{brine}\ge T_{i+1}^{brine}+\Delta T_{\min}^2\quad i<I\\ &T_i^{brine}\ge T_i^{feed}+\Delta T_{\min}^2\quad i=I\end{aligned} \tag{A.29}$$

$$\begin{aligned}&T_i^{distillate}\ge T_{i+1}^{brine}+\Delta T_{\min}^3\quad i<I\\ &T_i^{distillate}\ge T_i^{feed}+\Delta T_{\min}^3\quad i=I\end{aligned} \tag{A.30}$$

$$\begin{aligned}&T_i^{distillate}\ge T_i^{brine}+\Delta T_{\min}^4\quad i\in I\\ &T_i^{sat}\ge T_i^{brine}+\Delta T_{\min}^4\quad i\in I\end{aligned} \tag{A.31}$$

Appendix B. Correlations to estimate thermodynamic properties and boiling point elevation (BPE)

B.1 Fluid physical properties

The correlations for the estimation of fluid physical properties have been obtained by process simulations, using HYSYS-OLI under electrolytes thermodynamic package. These correlations are valid in ranges of $0\le X_i^{salt}\le 0.30$ and $10\le T_i\le 120$ °C. Thus, the correlation for estimating the fluids viscosity in each evaporator effect i is given by the following equation.

$$\mu_i = 0.001 \cdot \left(1.377 + 1.845 \cdot X_i^{salt} - 0.02301 \cdot T_i + 7.475 \cdot \left(X_i^{salt}\right)^2 - 0.03427 \cdot X_i^{salt} \cdot T_i + 0.0001418 \cdot (T_i)^2\right) \quad \forall i \in I \tag{B.1}$$

In which X_i^{salt} is the salt mass fraction in the evaporation effect i, and T_i indicates the stream temperature. The viscosity μ_i is expressed in kg (m s)$^{-1}$ and the temperature T_i in °C.

The streams thermal conductivities in the effect i are calculated by the following correlation.

$$\kappa_i = 0.001 \cdot \left(0.561 + 0.0017 \cdot T_i - 0.00000612 \cdot (T_i)^2\right) \quad \forall i \in I \tag{B.2}$$

In which κ_i is in kW (m K)$^{-1}$ and T_i in °C.

The specific heat calculation should consider the influences of the streams salinity and the temperature in an evaporator effect i. The specific heat is given by Eq. (B.3).

$$Cp_i = 4.118 - 4.757 \cdot X_i^{salt} + 0.001015 \cdot T_i \quad \forall i \in I \tag{B.3}$$

In which the specific heat Cp_i is expressed in kJ (kg °C)$^{-1}$ and the temperature T_i in °C.

The streams density in each evaporator effect i is calculated by Eq. (B.4).

$$\rho_i = 1016 + 719.6 \cdot X_i^{salt} - 0.672 \cdot T_i \quad \forall i \in I \tag{B.4}$$

In which the density ρ_i is in kg m^{-3} and T_i in °C.

Note that the physical properties expressed by the equations Eq. (B.1) to Eq. (B.4) are estimated by considering the liquid phase of the streams at the temperatures of condensation ($T_i^{distillate}$) and evaporation ($T_i^{boiling}$). For the calculation of the physical properties inside the tubes, it is considered that the condensate is salt free (*i.e.*, $X_i^{salt} = 0$).

The vaporization latent heat λ_i is estimated by the following correlation.

$$\lambda_i = 2502.5 - 2.3648 \cdot T_i^{sat} + 1.840 \cdot \left(T_{i-1}^{sat} - T_i^{sat}\right) \quad \forall i > 1 \tag{B.5}$$

In which the vaporization latent heat λ_i is expressed in kJ kg^{-1}. T_i^{sat} is the temperature of the saturated vapor in °C estimated by Eq. (B.6).

$$\ln\left(P_i^{sat}\right) = A + B/\left(T_i^{sat} + C\right) \quad \forall i \in I \tag{B.6}$$

In which P_i^{sat} is the saturation pressure in kPa. Moreover, A, B and C are the Antoine parameters that are equal to 12.98437, −2001.77468, and 139.61335, respectively. Eq. (B.6) also allows the estimation of the ideal temperature T_i^{ideal} (*i.e.*, the temperature that the effect i would have if its salinity is equal to zero) in the effect i. In this case, the vapor pressure P_i^{vapor} originated in the effect i is considered in Eq. (B.6).

The specific enthalpies for the liquid and vapor streams are estimated by the following correlations.

$$H_i^{vapor} = -13470 + 1.840 \cdot T_i^{boiling} \quad \forall i \in I \tag{B.7}$$

$$H_i^{liquid} = -15940 + 8787 \cdot X_i^{salt} + 3.557 \cdot T_i^{boiling} \quad \forall i \in I \tag{B.8}$$

In which the specific enthalpy H_i is in kJ kg^{-1}, and the boiling temperature $T_i^{boiling}$ is in °C. Note that the vapor and brine streams are considered to be at the same temperature $T_i^{boiling}$ in the evaporation effect i. In addition, the specific enthalpy of the feed water (shale gas produced water) in the last effect I can be estimated by Eq. (B.8), considering its feed temperature and salinity.

B.2 Boiling point elevation (BPE)

The boiling point elevation (BPE) is defined as the increase in the boiling temperature due to the salt concentration. The BPE is estimated by Eq. (B.9), considering the ideal temperature T_i^{ideal} and the salt mass fraction X_i^{salt} in the evaporation effect i.

$$BPE_i = \left(0.1581 + 2.769 \cdot X_i^{salt} - 0.002676 \cdot T_i^{ideal} + 41.78\left(X_i^{salt}\right)^{0.5} + 0.134 \cdot X_i^{salt} \cdot T_i^{ideal}\right) \quad \forall i \in I \tag{B.9}$$

References

Abraham, R., Mani, A., 2015. Heat transfer characteristics in horizontal tube bundles for falling film evaporation in multi-effect desalination system. Desalination 375, 129–137. http://dx.doi.org/10.1016/j.desal.2015.06.018.

Al-Juwayhel, F., El-Dessouky, H.M., Ettouney, H.M., 1997. Analysis of singleeffect evaporator desalination systems combined with vapor compression heat pumps. Desalination 253–275.

Al-Mutaz, I.S., 2015. Features of multi-effect evaporation desalination plants. Desalin. Water Treat. 54, 3227–3235. http://dx.doi.org/10.1080/19443994.2014.910842.

Al-Mutaz, I.S., Wazeer, I., 2014. Comparative performance evaluation of conventional multi-effect evaporation desalination processes. Appl. Therm. Eng. 73, 1194–1203. http://dx.doi.org/10.1016/j.applthermaleng.2014.09.025.

Chafidz, A., Kerme, E.D., Wazeer, I., Khalid, Y., Ajbar, A., Al-zahrani, S.M., 2016. Design and fabrication of a portable and hybrid solar-powered membrane distillation system. J. Clean. Prod. 133, 631–647. http://dx.doi.org/10.1016/j.jclepro.2016.05.127.

Chen, J.J.J., 1987. Comments on improvements on a replacement for the logarithmic mean. Chem. Eng. Sci. 42, 2488–2489. http://dx.doi.org/10.1016/0009-2509(87)80128-8.

Chen, H., Carter, K.E., 2016. Water usage for natural gas production through hydraulic fracturing in the United States from 2008 to 2014. J. Environ. Manag. 170, 152–159. http://dx.doi.org/10.1016/j.jenvman.2016.01.023.

Chen, G., Wang, Z., Nghiem, L.D., Li, X.M., Xie, M., Zhao, B., Zhang, M., Song, J., He, T., 2015. Treatment of shale gas drilling flowback fluids (SGDFs) by forward osmosis: membrane fouling and mitigation. Desalination 366, 113–120. http://dx.doi.org/10.1016/j.desal.2015.02.025.

Chung, H.W., Swaminathan, J., Warsinger, D.M., Lienhard, J.H., 2016. Multistage vacuum membrane distillation (MSVMD) systems for high salinity applications. J. Memb. Sci. 497, 128–141. http://dx.doi.org/10.1016/j.memsci.2015.09.009.

Clark, C.E., Horner, R.M., Harto, C.B., 2013. Life cycle water consumption for shale gas and conventional natural gas supporting information. Environ. Sci. Technol. 47, 1–9. http://dx.doi.org/10.1021/es4013855.

Couper, J.R., Penney, W.C., Fair, J.R., Walas, S.M., 2010. Chemical Process Equipment, Selection and Design, second ed. Elsevier, USA.

Drud, A.S., 1996. CONOPT: a System for Large Scale Nonlinear Optimization, Reference Manual for CONOPT Subroutine Library. ARKI Consulting and Development A/S, Bagsvaerd, Denmark.

Druetta, P., Aguirre, P., Mussati, S., 2013. Optimization of multi-effect evaporation desalination plants. Desalination 311, 1–15. http://dx.doi.org/10.1016/j.desal.2012.10.033.

Druetta, P., Aguirre, P., Mussati, S., 2014. Minimizing the total cost of multi effect evaporation systems for seawater desalination. Desalination 344, 431–445. http://dx.doi.org/10.1016/j.desal.2014.04.007.

El-Dessouky, H.M., Ettouney, H.M., 2002. Fundamentals of Salt Water Desalination, first ed. Elsevier.

El-Dessouky, H.M., Ettouney, H.M., Al-Juwayhel, F., 2000. Multiple effect evaporation-vapour compression desalination processes. Trans. IChemE 78, 662–676, 0263-8762/00/$10.00+0.00.

Ettouney, H.M., 2006. Design of single-effect mechanical vapor compression. Desalination 190, 1–15. http://dx.doi.org/10.1016/j.desal.2005.08.003.

Ettouney, H.M., El-Dessouky, H.M., Al-Atiqi, I., 1999. Understand thermal desalination. Chem. Eng. Prog. 95, 43–54.

European Comission, 2016. Eurostat.

Ghanbari, E., Dehghanpour, H., 2016. The fate of fracturing water: a field and simulation study. Fuel 163, 282–294. http://dx.doi.org/10.1016/j.fuel.2015.09.040.

Hammond, G.P., O'Grady, Á., 2016. Indicative energy technology assessment of UK shale gas extraction. Appl. Energy. http://dx.doi.org/10.1016/j.apenergy.2016.02.024 (in press).

Han, D., He, W.F., Yue, C., Pu, W.H., 2016. Study on desalination of zero-emission

system based on mechanical vapor compression. Appl. Energy. http://dx.doi.org/10.1016/j.apenergy.2015.12.061.
He, C., Wang, X., Liu, W., Barbot, E., Vidic, R.D., 2014. Micro fi ltration in recycling of Marcellus Shale flowback water: solids removal and potential fouling of polymeric micro filtration membranes. J. Memb. Sci. 462, 88–95. http://dx.doi.org/10.1016/j.memsci.2014.03.035.
Huang, L., Fan, H., Xie, H., Huang, Z., 2016. Experimental study of treatment processes for shale gas fracturing flowback fluid in the eastern Sichuan Basin. Desalin. Water Treat. 3994, 1–14. http://dx.doi.org/10.1080/19443994.2016.1141714.
Li, W., Wu, X.Y., Luo, Z., Yao, S.C., Xu, J.L., 2011. Heat transfer characteristics of falling film evaporation on horizontal tube arrays. Int. J. Heat. Mass Transf. 54, 1986–1993. http://dx.doi.org/10.1016/j.ijheatmasstransfer.2010.12.031.
Lira-Barragán, L.F., Ponce-Ortega, J.M., Guillén-Gosálbez, G., El-Halwagi, M.M., 2016. Optimal water management under uncertainty for shale gas production. Ind. Eng. Chem. Res. 55, 1322–1335. http://dx.doi.org/10.1021/acs.iecr.5b02748.
Mussati, S., Scenna, N., Tarifa, E., Franco, S., Hernandez, J.A., 2009. Optimization of the mechanical vapor compression (MVC) desalination process using mathematical programming. Desalin. Water Treat. 5, 124–131. http://dx.doi.org/10.5004/dwt.2009.572.
Nafey, A.S., Fath, H.E.S., Mabrouk, A.A., 2006. Thermoeconomic analysys of multi stage flash-thermal vapor compression (MSF-TVC) desalination process. In: Tenth International Water Technology Conference, pp. 189–203.
Nicot, J.-P., Scanlon, B.R., 2012. Water use for shale gas production in Texas. U.S. Environ. Sci. Technol. 46, 3580–3586. http://dx.doi.org/10.1021/es204602t.
Onishi V.C., Carrero-Parreño A., Reyes-Labarta J.A., Ruiz-Femenia R., Salcedo-Díaz R., Fraga E.S. and Caballero J.A., Shale gas flowback water desalination: single *vs* multiple-effect evaporation with vapor recompression cycle and thermal integration, Desalination, (in press)
Qiu, Q., Zhu, X., Mu, L., Shen, S., 2015. Numerical study of falling film thickness over fully wetted horizontal round tube. Int. J. Heat. Mass Transf. 84, 893–897. http://dx.doi.org/10.1016/j.ijheatmasstransfer.2015.01.024.
Shaffer, D.L., Arias Chavez, L.H., Ben-Sasson, M., Romero-Vargas Castrillón, S., Yip, N.Y., Elimelech, M., 2013. Desalination and reuse of high-salinity shale gas produced water: drivers, technologies, and future directions. Environ. Sci. Technol. 47, 9569–9583. http://dx.doi.org/10.1021/es401966e.
Shen, S., Liu, H., Gong, L., Yang, Y., Liu, R., 2014. Thermal analysis of heat transfer performance in a horizontal tube bundle. Desalin. Water Treat. 54, 1809–1818. http://dx.doi.org/10.1080/19443994.2014.895780.
Shen, S., Mu, X., Yang, Y., Liang, G., Liu, X., 2015. Experimental investigation on heat transfer in horizontal-tube falling-film evaporator. Desalin. Water Treat. 56, 1440–1446. http://dx.doi.org/10.1080/19443994.2014.949604.
Smith, R.M., 2005. Chemical Process Design and Integration, second ed. John Wiley and Sons Ltd, England.
Staddon, P.L., Depledge, M.H., 2015. Fracking cannot be reconciled with climate change mitigation policies. Environ. Sci. Technol. 8269–8270. http://dx.doi.org/10.1021/acs.est.5b02441.
Thu, K., Kim, Y.-D., Shahzad, M.W., Saththasivam, J., Ng, K.C., 2015. Performance investigation of an advanced multi-effect adsorption desalination (MEAD) cycle. Appl. Energy 159, 469–477. http://dx.doi.org/10.1016/j.apenergy.2015.09.035.
Turton, R.C., Bailie, R.C., Whiting, W.B., 2012. Analysis, Synthesis, and Design of Chemical Processes, fourth ed.
Walmsley, T.G., 2016. A Total Site Heat Integration design method for integrated evaporation systems including vapour recompression. J. Clean. Prod. 136, 111–118. http://dx.doi.org/10.1016/j.jclepro.2016.06.044.
Xiong, B., Zydney, A.L., Kumar, M., 2016. Fouling of microfiltration membranes by flowback and produced waters from the Marcellus shale gas play. Water Res. 99, 162–170. http://dx.doi.org/10.1016/j.watres.2016.04.049.
Zammerilli, A., Murray, R.C., Davis, T., Littlefield, J., 2014. Environmental Impacts of Unconventional Natural Gas Development and Production, vol. 800, 553–7681.
Zhang, X., Sun, A.Y., Duncan, I.J., 2016. Shale gas wastewater management under uncertainty. J. Environ. Manag. 165, 188–198. http://dx.doi.org/10.1016/j.jenvman.2015.09.038.
Zhao, C.-Y., Ji, W.-T., Jin, P.-H., Tao, W.-Q., 2016. Heat transfer correlation of the falling film evaporation on a single horizontal smooth tube. Appl. Therm. Eng. 103, 177–186. http://dx.doi.org/10.1016/j.applthermaleng.2016.02.090.
Zhou, S., Guo, Y., Mu, X., Shen, S., 2015. Effect of design parameters on thermodynamic losses of the heat transfer process in LT-MEE desalination plant. Desalination 375, 40–47. http://dx.doi.org/10.1016/j.desal.2015.07.015.